Multiphoton population transfer in systems violating the classical twist condition: A comparative study of separatrix crossing in phase space

Turker Topcu and Francis Robicheaux
Department of Physics, Auburn University, Alabama 36849-5311, USA
(Received 15 December 2010; published 27 April 2011)

Population transfer in Hamiltonian systems, such as between Rydberg states of atoms and vibrational modes in diatomic molecules, has been both experimentally and theoretically demonstrated. All these systems have the property that the classical frequency of the motion changes monotonically with energy. Referred to as the twist condition, this property makes it possible to transfer population both by chirping a driving field within a ladder climbing scheme and by adiabatically chirping through a multiphoton resonance connecting two bound states. In this paper, we demonstrate that the latter method for population transfer can still be made to work in a system which violates the classical twist condition. We use classical rigid rotor as an example system where the frequency changes monotonically with energy and compare the responsible separatrix crossing mechanism in phase space to that in a system which exhibits an extremum in the frequency-energy profile. We perform both one-dimensional classical and quantum simulations and find that the quantum phase-space distribution mirrors its corresponding classical counterpart.

DOI: 10.1103/PhysRevE.83.046607 PACS number(s): 33.80.Rv, 05.45.Pq

I. INTRODUCTION

As an indispensable tool in manipulation of atomic and molecular systems, population transfer between bound states of atoms and vibrational modes of molecules has received a lot of attention from both experimental and theoretical fronts. From the molecular perspective, preparation of advantageous initial vibrational modes has been important in endeavors toward molecular imaging using strong laser fields through high-harmonic generation and electron rescattering [1]. There are also experimental efforts to use molecules for quantum computation research by exploiting vibrational-electronic coupling, which requires controlling and manipulating vibrational modes [2]. Interest in atomic control has also long stemmed from the same venues as well as more classical problems especially in Rydberg physics, such as creating Bohr-like wave packets for precision spectroscopy and studying classical-quantum correspondence (see Ref. [3] and references therein).

There have been mainly two robust methods for inducing transitions between excited bound states of such systems: the most common method is referred to as the "ladder-climbing" scheme in which a population of initial state is carried through many single photon transitions by adiabatically chirping a laser field [4]. Classically, this can be achieved by driving the system on resonance with the initial ensemble of trajectories in phase space, creating an island of stability onto which the trajectories can be loaded. Then by adiabatically chirping the laser frequency, this island can be dragged around the phase space, carrying with it the trapped population of classical trajectories to a desired region in phase space, which may correspond to a higher excited state. The second method is the multiphoton adiabatic rapid passage, which works by adiabatically chirping through a multiphoton resonance between an initial and a final state. The latter has recently been subject to experimental and theoretical studies, which demonstrated its effectiveness in transferring population between Rydberg states in Li atom using microwaves [5,6] and trains of impulsive kicks [7]. Furthermore, the same method has been theoretically demonstrated for inducing efficient multiphoton transitions between vibrational modes of diatomic molecules [8]. These studies have revealed that such multiphoton transitions can be explained by a separatrix crossing mechanism taking place in classical phase space, in addition to the traditional quantum Floquet picture.

All of these systems have a common physical characteristic: They are all closed Hamiltonian systems where the frequency changes monotonically with energy. Quantum mechanically, this would correspond to monotonically changing adjacent energy level *spacings* with energy. This is commonly referred to as the classical *twist condition*, which is very commonly conformed to among mostly studied Hamiltonian systems (see Ref. [9] and references therein). In the case of population transfer using the ladder scheme, the fact that atoms conform to the twist condition is vital for the method to work. Since the main idea behind this method is to chirp the driving laser between the initial and the final states, violation of the twist condition at some frequency, which needs to be traversed during the chirping, would mean to reverse the direction of the chirp. This would take the population back down closer to the initial state, preventing the ladder climbing scheme from being useful.

However, what happens in a system violating the twist condition, a nontwist system, when the multiphoton adiabatic rapid passage scheme is used is not trivial. In this method, chirping of the driving laser is not essential for the physical mechanism taking place in the classical phase space [5]. Rather, chirping here only enhances the efficiency of the population transfer. The classical phase-space structure of nontwist maps has been extensively studied in Hamiltonian systems [10,11], particularly with connection to magnetic field lines and reconnection [12]. These studies have revealed that in such systems, phase space is divided into regions separated by a *shearless* curve, a curve along which the twist condition is violated. When such a system is driven close to the frequency at which the frequency-energy profile exhibits an extremum, two sets of stable islands are formed

above and below the shearless curve. As the driving strength is increased, separatrices associated with these islands may change topology and go from being heteroclinic (X points) to homoclinic (O points), resulting in rich and interesting dynamics in the classical phase space. Whether the previously studied multiphoton population transfer scheme would work in such a system to transfer population between classical actions separated by the shearless curve in phase space is the question we will investigate in this paper.

Beyond magnetic reconnection, the nontwist condition may also be induced in atomic Rydberg systems. Younge *et al.* have demonstrated that state-dependent shifts in atomic energy levels can be induced by ponderomotive potentials experienced by atoms in optical lattices [13]. The direction and the magnitude of the shifts experienced by the energy levels strongly depend on the state and result from an aspect ratio between the size of the atom and the optical lattice period. They observe a 50-MHz shift for $n = 50$ state of Rb atom, which is roughly three orders of magnitude smaller than the energy spacing between the n levels adjacent to $n = 50$. Although this is not a large enough shift to induce an extremum in the otherwise monotonically changing energy spectrum with n, it suggests that it may be possible to engineer ponderomotive potentials that for a very large n could potentially induce a bound-state structure which violates the twist condition.

The paper is organized as follows: in Sec. II, we study the classical separatrix crossing mechanism in one-dimensional rigid rotor in the multiphoton population transfer context, as an example system conforming to the classical twist condition. This will serve as a case for comparison when we investigate a particle in a potential well which violates the twist condition in Sec. III. In Sec. III, we describe this system and our one-dimensional classical and quantum simulations of population transfer in this system. We find that the multiphoton population transfer scheme can be made to work to transfer population across the shearless curve and describe the underlying separatrix crossing mechanism responsible for the transfer. Our quantum simulations also reveal that the same classical phase-space mechanism is at play in quantum phase-space distribution.

We use atomic units throughout the paper unless we explicitly specify other units.

II. CLASSICAL RIGID ROTOR IN ONE DIMENSION

In this section, we demonstrate the classical separatrix crossing idea behind the multiphoton adiabatic rapid passage observed in Rydberg atoms [5–7] using a one-dimensional rigid rotor. Just as in a Rydberg atom with essentially one active electron, in a rigid rotor, frequency changes monotonically with energy. The only difference is that the frequency increases with energy in a rotor, whereas it decreases with electronic energy in an atom. This nonmonotonicity of frequency ω can be expressed as

$$\frac{\partial \omega(J)}{\partial J} \neq 0, \tag{1}$$

which is referred to as the twist condition in Hamiltonian systems. Here J is the classical action and corresponds to the principal quantum number n in an atom and to angular momentum L in a rigid rotor. In the latter case, this translates into energy as $E(L) = L^2/(2I)$, where I is the moment of inertia, i.e., mR^2 with m being the mass and R being the radius of rotation. We assume the Hamiltonian for a one-dimensional rigid rotor in the presence of periodic driving to be

$$H(x,p,t) = p^2/2m + F(t)R\cos(x), \tag{2}$$

$$F(t) = F_0 \exp[-(t/t_W)^2]\cos(\omega t), \tag{3}$$

where x and p are the usual position and linear momentum coordinates in one dimension and $F(t)$ is the time dependence of the periodic driving. The driving field is enveloped inside a Gaussian with a width of t_W and has the amplitude F_0. The corresponding classical force is

$$F_x = -\frac{dV(x,t)}{dx} = F(t)R\sin(x), \tag{4}$$

with $V(x,t) = F(t)R\cos(x)$ and the period of the classical motion is $T = 2\pi R/\sqrt{2E/m}$. In the following simulations, we assume a rigid rotor with $m = 1$ a.u. and $R = 1$ a.u. of length.

In order to illustrate the classical transition through separatrix crossing in a rigid rotor, we solve Hamilton's equations using a fourth-order adaptive step-size Runga-Kutta method as described in detail in Ref. [5] using the Hamiltonian in Ref. [8]. We assume two different transitions when the rotor starts with an angular momentum of 12 a.u. and is driven to be exactly resonant with a 4-photon and a 10-photon resonance, connecting $L = 12$ with $L = 16$ and 22 respectively. The resulting angular momentum distributions after a pulse of 168 periods of the rigid rotor at full width at half maximum (FWHM) for three different driving field intensities, is seen in Fig. 1.

The upper panel in Fig. 1 shows the probabilities P to find the rotor in L up to 24 for peak driving field intensities of 2.5×10^{10} W/cm^2 (squares), 3.0×10^{10} W/cm^2 (circles), and 4.8×10^{10} W/cm^2 (triangles). We have found that for peak field intensities less than 2.5×10^{10} W/cm^2, the rotor stays in its initial classical state with no change in its angular momentum or classical action. When the peak field intensity is increased to 3.0×10^{10} W/cm^2, roughly 80% of the population jumps up to $L = 16$, remaining ~20% staying in the initial state of $L = 12$. Further increase of the intensity up to 4.8×10^{10} W/cm^2 does not increase the amount transferred into $L = 16$ but rather spreads the population over a broad range of angular momentum, which still peaks at $L = 12$ with $P \sim 0.2$ and $L = 16$ with $P \sim 0.35$.

The lower panel in Fig. 1 depicts the case when the rotor is driven in resonance with a 10-photon transition which would take it from $L = 12$ to $L = 22$, using the same Gaussian pulse width as in the upper panel. The peak field intensities of 1.4×10^{11} W/cm^2, 1.8×10^{11} W/cm^2, and 3.8×10^{11} W/cm^2 are labeled as the squares, circles, and triangles, respectively. For field intensities less than 1.4×10^{11} W/cm^2 we observe no transitions into higher angular momenta, whereas we see about 60% transition into $L = 22$ for 1.8×10^{11} W/cm^2 with no spread over other angular momenta. For the higher intensity of 3.8×10^{11} W/cm^2, the population spreads over angular momenta, again peaking at the initial $L = 12$ and the intended final angular momentum of 22. The higher-order 10-photon

transition is harder to achieve at the same level of efficiency as the 4-photon transition as the jump required in energy is higher as well as the number of photons that need to absorbed in the quantum-mechanical picture.

Although this kind of multiphoton transition process can easily be explained in the quantum-mechanical resonance picture, Fig. 1 requires a classical process since there are no classical resonances corresponding to discrete values of angular momentum, as L is a continuous variable in classical mechanics. The process which makes this multiphoton transition classically possible can be explained by investigating the classical phase space in the standard action-angle (J,θ) variables, as was done for Rydberg atoms in the past [5,7]. The canonical action-angle variables corresponding to the Cartesian (x,p) coordinates are (L,θ), where θ is the angular position of a rigid rotor, i.e., $\theta = R\cos(x)$. For the 10-photon transition with the peak field intensity of 1.8×10^{11} W/cm^2 seen as circles in the lower panel of Fig. 1, the surfaces of section plots in action-angle variables are seen in Fig. 2. Three panels from top to bottom are snapshots in time at points in the rising edge, at the peak, and the falling edge of the Gaussian field envelope. The dark points show the phase-space positions of an ensemble of trajectories which start out with a fixed classical action or angular momentum of 12. In Figs. 2(a) and 2(c), the field strengths are 1/8 of the peak field strength

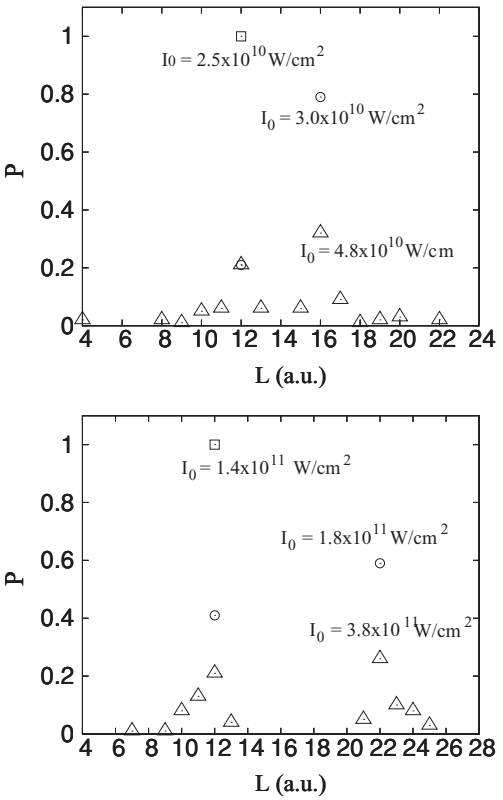

FIG. 1. Final population distribution in a one-dimensional rigid rotor with an initial angular momentum of $L = 12$ driven at 4-photon (upper panel) and 10-photon (lower panel) resonance frequencies. The 4-photon resonance takes the rotor up to $L = 16$ and the 10-photon case takes it up to $L = 22$. In each case, results for three different peak field intensities are shown, all of which are using a pulse with a width of 168 periods at FWHM.

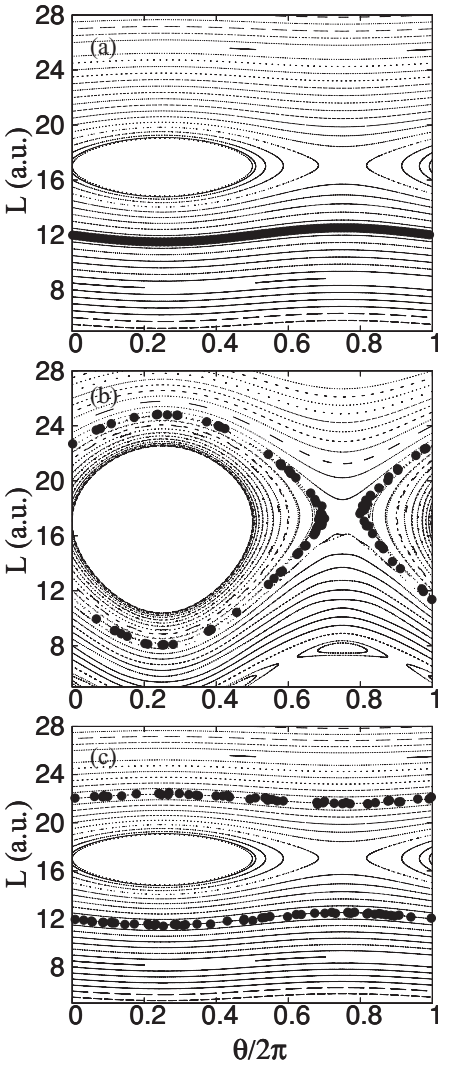

FIG. 2. Classical phase-space structure for the one-dimensional rigid rotor driven from $L = 12$ to 22 at the 10-photon resonance with a peak intensity of $I_0 = 1.8 \times 10^{11}$ W/cm^2 seen in the lower panel of Fig. 1. Panels (a) and (c) are snapshots in time during the rising and falling edges of the Gaussian pulse envelope at intensities 2.26×10^{10} W/cm^2 and the middle panel is at the peak of the pulse. Larger points mark the phase-space coordinates of the classical trajectories, initially loaded onto the $L = 12$ line as seen in (a). As the field intensity is increased, the island created at the driving frequency grows larger and eventually touches the $L = 12$ line, resulting in transportation of the trajectories on the $L = 12$ line to above the island. As the field is decreased back down, substantial fraction of the population ends up in $L = 22$ as seen in (c).

corresponding to 1.8×10^{11} W/cm^2 peak field intensity. Note that in Fig. 1(a), the trajectories are still on the $L = 12$ surface as an island of stability is formed at the angular momentum corresponding to the driving frequency, although the driving is not yet strong enough for the island to become large enough to touch the $L = 12$ surface. As the peak intensity is reached in Fig. 2(b), the island of stability has become large enough, and some of the trajectories that were initially on the $L = 12$ surface have moved across the island onto the $L = 22$ surface by passing through the separatrix that connects the L surfaces

above the island with those below it. As the field is ramped back down such that the field strength is again 1/8 of that at the peak in Fig. 2(b), the island of stability has shrunk back to its size in Fig. 2(a), once again isolating the $L = 12$ and $L = 22$ surfaces. Roughly 60% of the population ends up on the $L = 22$ surface and the remaining stays on $L = 12$, as was seen on the lower panel of Fig. 1.

III. PARTICLE IN ONE-DIMENSIONAL POTENTIAL WELL: VIOLATION OF THE CLASSICAL TWIST CONDITION

We now consider a physical system in which the classical twist condition of Eq. (1) is violated. In such a system, the classical frequency ω would exhibit an extremum as a function of classical action since, violation of Eq. (1) would mean $\partial\omega(J)/\partial J = 0$. From the quantum-mechanical standpoint, this could be thought as a system exhibiting frequencies which may first increase and then decrease with increasing energy E or corresponding principal quantum number n. As an example of such a system, we consider a particle in a potential well described by

$$U(x) = A\exp[-(x/D)^4], \tag{5}$$

where A is the depth of the potential well and D is its width. The corresponding classical force is $F_x = -dU(x)/dx = 4x^3U(x)/D^4$, and the acceleration is $a_x = F_x/m$. In our simulations below, we assume that $A = -2.0$ a.u. and $D = 200$ a.u., and the particle has a mass of $m = 2$ a.u.. This describes a potential well with an approximately flat bottom so when the particle is at the bottom of the well, it has a very low frequency, just as it would just above the ionization threshold at $U(x = 0) = 0$. Having higher frequencies in between the bottom and the top of the well would mean that the energy spectrum has to exhibit an extremum in between, violating the twist condition. The classical frequency profile for this particle can be seen in Fig. 3 both as a function of energy and the classical action $J/2\pi$, which approximately corresponds to the quantum-mechanical principal quantum number n. The frequency has a maximum at around $n \sim 100$, at which point $\partial\omega(J)/\partial J$ vanishes. Fig. 3 makes it clear that if we start out with an ensemble of trajectories (or equivalently with a quantum state) with $n < 100$ and wish to transfer population to a state with $n > 100$ via usual means of population transfer, such as ladder climbing, we would run into a problem at the peak of the frequency profile at $n \sim 100$. Chirping the driving laser frequency from that of the initial-state to the final-state frequency, we would have chirp through the frequency corresponding to that at the peak at $n \sim 100$. At this point, chirping the frequency up to higher pitch does nothing since there are no corresponding frequencies in the spectrum. Similarly, chirping the frequency down after this point would just guide the population back down to its initial state through the same path it came up. What happens as a result of this violation of the twist condition and if it is at all possible to transfer any population to states beyond the maximum at $n \sim 100$ are the questions we would like to investigate. For this purpose, we will try to transfer population by driving the system at a multiphoton

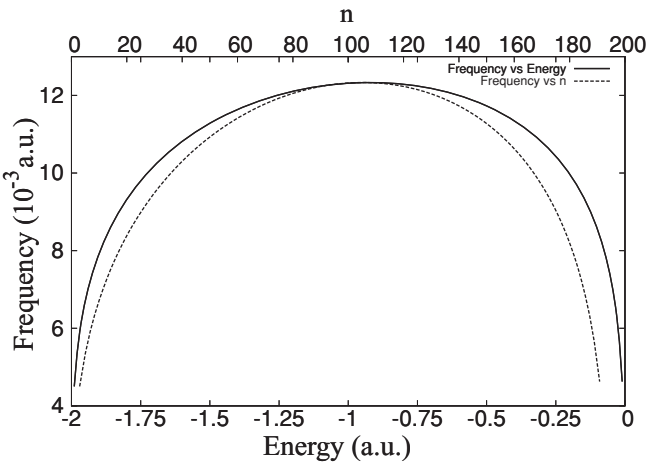

FIG. 3. Frequency versus energy (solid line) and frequency versus n (dashed line) for the potential $U(x) = A\exp[-(x/D)^4]$ with $A = -2.0$ a.u., $D = 100$ a.u., and $m = 2.0$ a.u.. The classical action is $2\pi n$, where n approximately corresponds to principal quantum number. The frequency ~0.0122 at the peak around $n \sim 100$ is where the classical twist condition breaks down.

resonance and investigate what happens from both classical and quantum-mechanical standpoints.

A. Classical simulations in one dimension

To study the underlying classical processes taking place, we will peek into the classical phase space as we did in the previous section. The canonical action-angle variables (J,θ) for our system are evaluated from the Cartesian $(x\text{-}p)$ coordinates as follows through the usual definitions for the action and angle variables:

$$J = \oint mv\,dx, \tag{6}$$

$$\theta/2\pi = \frac{t}{T} = \int_{x_1}^{-x} \frac{dx}{v(x)}. \tag{7}$$

Here v is the velocity of the particle, T is the period of its motion, and t is time. We employ Chebyshev integration to evaluate the action integral between the turning points $x_{1,2} = \pm D[-\ln(E/A)]^{1/4}$, and a square-root mesh to calculate the angle variable. From Bohr quantization, the classical action approximately corresponds to $2\pi n$, where n is the principal quantum number.

The Poincare surfaces of section in phase space when the system is driven with frequency $\omega_c = 0.0122$ a.u. at four different field strengths can be seen in Fig. 4. This frequency is just below the peak seen in Fig. 3. Overlayed with the surfaces of section are the phase-space positions of trajectories which were initially launched at $E = -1.27$ a.u., energy corresponding to $n = 80$. In a field of 1.2×10^{-5} a.u., two islands of stability are formed at two degenerate principal quantum numbers corresponding to the driving frequency ω_c just below and above the peak in Fig. 3. Circles A and B mark the heteroclinic separatrices (also called X points) for the two sets of islands below and above the the peak of the classical action at $n \sim 100$. The islands of stability recur along

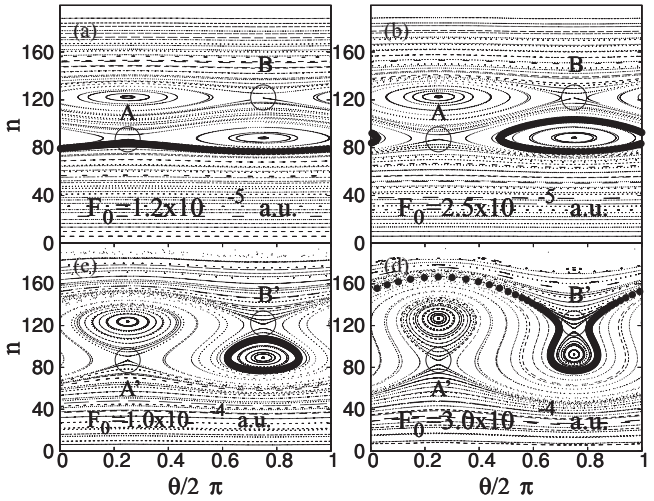

FIG. 4. Classical phase-space structures for the nontwist system in action ($2\pi n$) and angle variables with $E = -1.27$ a.u. and driving frequency 0.0122 a.u., when the system is driven at four different field strengths. Similarly to Fig. 2, the larger black points show the phase-space coordinates of the microcanonical ensemble initially loaded onto $n = 80$. In the upper two panels, (a) and (b), the circles mark the heteroclinic separatrices formed by the increasing field strength. The trajectories on the $n = 80$ line in (a) hop onto the island below the shearless curve in (b) as a result of a reconnection in separatrix A caused by the higher field strength. In (c), the field is strong enough such that the heteroclinic separatrices A and B become homoclinic as marked by the circles A' and B'. Finally, in (d), the stronger driving causes a reconnection in the upper separatrix B', making the upper region of the phase space accessible to the trajectories that were captured onto the lower island in (b).

the direction of the scaled angle variable $\theta/2\pi$ at both n with frequency ω_c. The region between the these two sets of islands corresponds to the classical n range between the degenerate n values with frequency ω_c straddling the peak at $n \sim 100$ in Fig. 3. The actual line corresponding to the peak value of the classical action around $n \sim 100$ is referred to as the *shearless curve*. Along this curve, the rotation number, which is defined as the horizontal jump a trajectory makes as it pierces through the surface of section, is zero. In other words, $dE(n)/dn = 0$, meaning that the trajectory on this curve does not drift in the θ direction as it is strobed at the driving frequency ω_c. The lines above and below the shearless curve either have $dE(n)/dn < 0$ or $dE(n)/dn > 0$, making the trajectories drift either to the left or to the right in the horizontal direction. This is again evident from Fig. 3 as the tangent of the energy-frequency profile changes sign as energy is traversed through the peak at roughly $n \sim 100$. As the energy-frequency curve gets steeper farther away from the peak, i.e., as $dE(n)/dn$ gets larger in magnitude, the drift of the trajectories in the horizontal direction in phase space speeds up further down and further up from the shearless curve, albeit in the opposite directions.

As the driving field strength is increased to 2.5×10^{-5} a.u. in Fig. 3(b), the islands of stability grow larger as the stable surfaces straddling the islands merge into the islands. This results in the shrinkage of the band of stable surfaces separating the islands above and below the shearless curve as these lines merge into the islands from above and below toward the shearless curve. Phase-space positions of the microcanonical ensemble of classical trajectories initially loaded onto the $n = 80$ line seen in Fig. 3(a) are now captured onto the island below the shearless curve, meaning that the $n = 80$ surface has merged into the island above it as it expanded. The two heteroclinic separatrices A and B are somewhat more prominent in this case compared to the weaker driven case in Fig. 3(a).

Further increase in the driving field strength to 1.0×10^{-4} a.u. in Fig. 4(c) results in a drastic topological transformation of the heteroclinic separatrices A and B seen in Figs. 4(a) and 4(b). As the driving field strength is ramped up, the stable surfaces just below and above the shearless curve keep merging into the main islands, eventually almost only leaving the shearless curve separating the two sets of islands above and below it. This morphs the the phase-space topology such that the initially heteroclinic separatrices A and B now become homoclinic. We label the new homoclinic separatrices (also called O points) A' and B' in Fig. 4(c). The microcanonical ensemble of trajectories we have been following are still seen on the island below the shearless curve at this driving field strength as they were in Fig. 4(b).

For the highest field strength we consider in Fig. 4(d), the phase-space positions of these trajectories which were initially loaded onto $n = 80$ in Fig. 4(a) now lay on a line which straddles the island with the homoclinic separatrix B'. This line stretches from below the island on the right to above the island on the left, spanning an n range from $n \sim 80$ to more than 160. We have observed that the phase-space positions of these trajectories drift in θ coordinate in time, suggesting that this line is not the shearless boundary but still a line which lay close to it. This hints to us that by turning off the driving field at the right time, it may be possible to transfer a substantial fraction of the initial ensemble to an n range above the shearless curve, i.e., beyond the peak of the frequency profile in Fig. 3.

Before we continue with the discussion of our classical simulations any further, we explain our quantum-mechanical simulations, as we contrast both in our later discussions.

B. Quantum calculations in one dimension

A detailed account of our numerical methodology for our one-dimensional quantum calculations has been given in Ref. [8] for the case of an IR driven diatomic molecule. We solve the one-dimensional time-dependent Schrödinger equation using a lowest-order implicit scheme using a uniform mesh in space. We use the Hamiltonian

$$H(x,p,t) = p^2/2m + U(x) + F(t)x, \tag{8}$$

where $U(x)$ is the same potential we used in our classical simulations in Sec. III A and $F(t)$ is identical to the one used in Eq. (2). We employ a radial mesh in space that extends from -250 a.u. to 250 a.u. using 4500 mesh points, which results in eigenenergies accurate to within roughly a part in 10^5. This is particularly important since change in the energy spacing between adjacent n states around the peak in Fig. 3 is small. For instance, the energy separation between $n = 99$ and $n = 100$ is 0.01231 a.u. compared to 0.01232 a.u. between $n = 101$ and $n = 100$. The time step taken during the propagation of the

Schrödinger equation is 5×10^{-5} times the classical period τ between the turning points for the energy of the initial state. We quote the driving pulse widths in units of τ in our discussions. In all of our simulations below, we start in the $n = 80$ state and drive the system at $\omega_c = 0.0122$, which corresponds to the energy spacing between $n = 100$ and $n = 99$ roughly within a part in 10^5. This is just below the peak in Fig. 3.

What happens to the quantum-mechanical counterpart of the classical system described in Sec. III A when driven by an electric field with peak field strength 7.0×10^{-5} a.u. is seen in Fig. 5. Here the Gaussian driving field envelope has a width of 90τ. For ease of picturing the migration of the initial-state population, we have integrated the probability of finding the system in a particular n state between $n = 70$–90 (solid curve), 90–110 (dashed curve), and 110–130 (dotted curve). The solid curve starts at unity since the system starts out entirely in $n = 80$. As the peak of the driving field envelope nears, the system moves out of the P_{70-90} band and enters into the P_{90-110} band. The initial band P_{70-90} sharply drops to almost nothing right after the pulse peak at $t = 0$ a.u., and almost the entire population crosses first into the middle P_{90-110} band, and then into the upper $P_{110-130}$ band. The fraction of the population residing inside the upper $P_{110-130}$ band becomes maximum at the pulse peak around 75%, at which point the total probability in both the middle and the lower bands exhibit a minimum. Soon after the pulse peak, the probability of finding the system in the upper n-band quickly drops as P_{90-110} recovers. P_{90-110} peaks again as roughly 75% of the system is in the middle n-band. Finally, the population returns back to the initial P_{70-90} band by the end of the pulse. Figure 5 shows periodic migration of the probability between the initial lower n-band and an upper band, while the middle n-band is crossed twice in one period. This is in parallel with our previous discussion of Fig. 4(d), where the phase-space positions of the trajectories lay on a stable line extending from roughly $n \sim 80$ to $n \sim 160$ for a much stronger driving field of 4.0×10^{-4} a.u.. As the trajectories did not lay on the shearless curve but rather below it in Fig. 4(d), the phase-space positions of these trajectories drift in time with different angular speed depending on where they are vertically in the phase space. This results in the oscillation of population below and above the stable islands in Fig. 4. The same situation is quantum mechanically realized in Fig. 5, as the lower band of n states represents region just below, and the upper band represents the region just above the islands in Fig. 4. The middle n-band corresponds to a region which house the shearless curve.

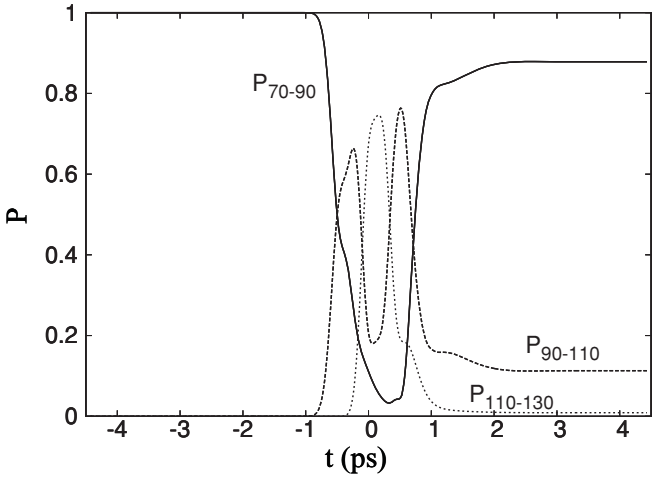

FIG. 5. Time dependence of the quantum probabilities to find the system within three adjacent n-bands. The system initially starts as a microcanonical ensemble with $n = 80$ and is driven by a Gaussian pulse with a width of 90τ at FWHM and a peak field strength of 7.0×10^{-5} a.u. at $\omega_c = 0.0122$ a.u., just below the peak in Fig. 3. The oscillations in three curves suggest that the substantial fraction of the population is transferred up into the $n = 110$–120 band by the peak of the pulse, and roughly 90% of it returned back to the initial $n = 70$–90 band, exhibiting a full period of oscillation between the upper and the lower n-bands.

The upper panel in Fig. 6 depicts the time dependence of the n distribution for the same driving pulse as the one in Fig. 5 with a width of 90τ at FWHM. The lower panel is for the exact same set of parameters except the width of the pulse is 25τ. In both cases, the system starts out in $n = 80$

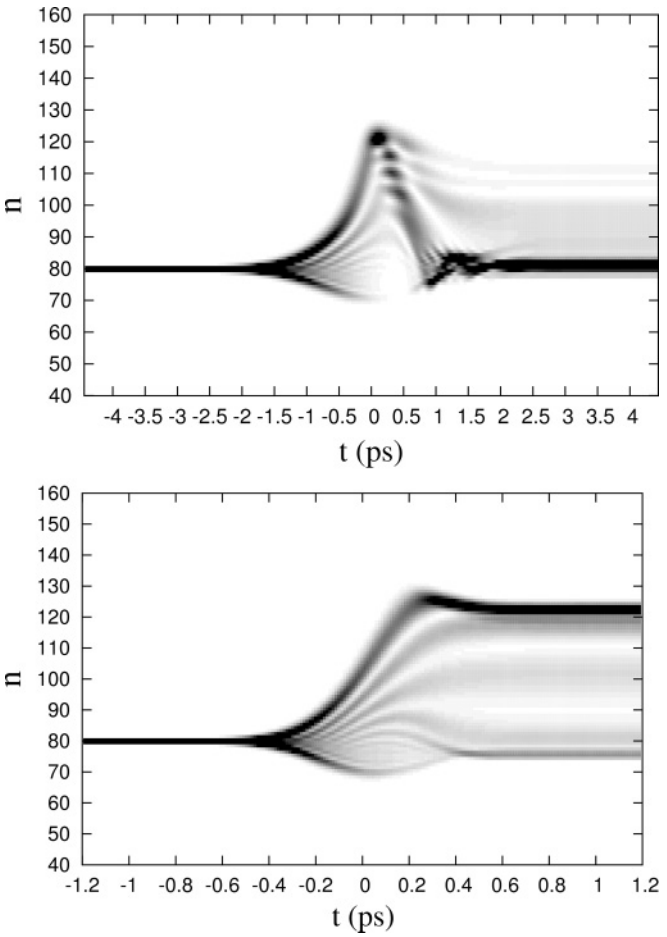

FIG. 6. Time dependence of the n distributions in the nontwist system driven by pulses with widths 90τ and 25τ at the same frequency and the peak field strength as in Fig. 5 from quantum simulations. The upper panel clearly shows the population going up in n and reaching $n \sim 120$ before returning back down to a small spread around the initial state $n = 80$ as indicated in Fig. 5. The shorter pulse in the lower panel, however, does not give enough time for the population to come back down from $n \sim 120$, leaving almost the entire population in a small spread around $n = 120$.

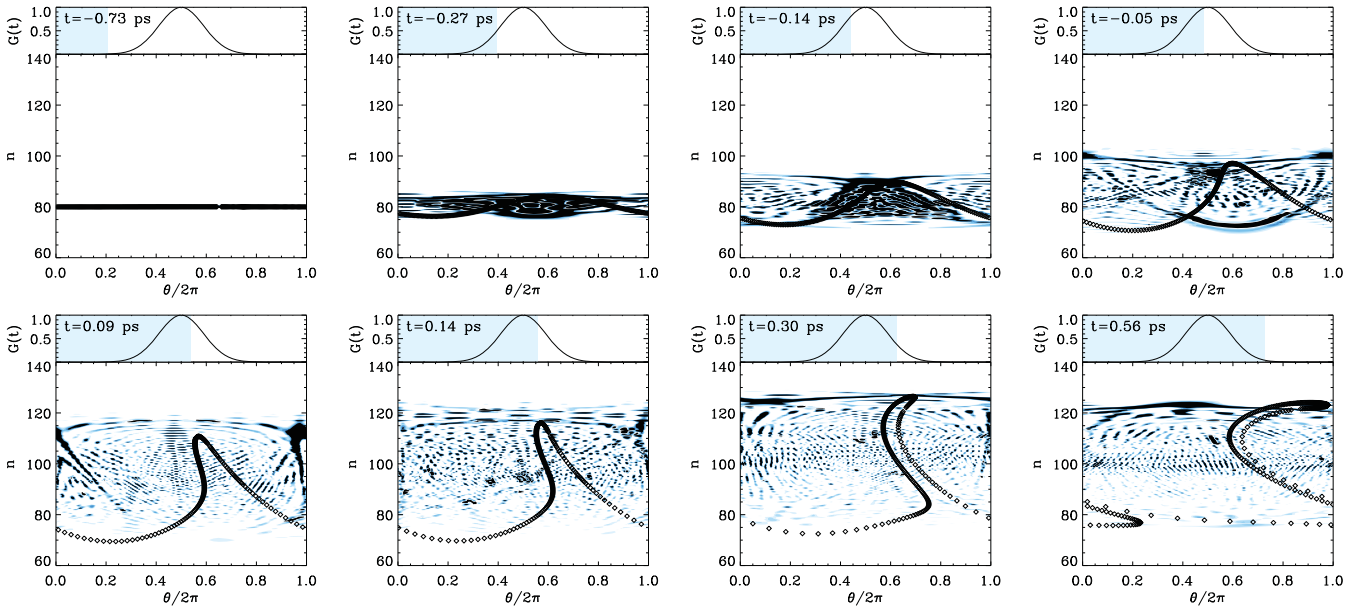

FIG. 7. (Color online) Snapshots of classical phase-space positions of the trajectories and the quantum Wigner distribution at different points during the field pulse as shown in the upper panel of each figure. The driving frequency and the pulse parameters are same as those in Fig. 6. The phase space is represented in action-angle variables as usual and the classical trajectories are depicted by the black points. The system starts out in $n = 80$ at $t = -0.73$ ps and the classical trajectories make their way up to $n \sim 120$ shortly after the pulse peak. The quantum phase-space density clearly mirrors the classical phase-space positions of the trajectories. At the end of the pulse majority of the population ends up at $n \sim 120$ as in the lower panel in Fig. 6.

and as the field strength becomes large enough, most of the probability migrates up in n up to $n \sim 120$ just until after the peak of the pulse. For the wider pulse width of 90τ at FWHM, the probability bounces back to $n \sim 80$ by the end of the pulse, as depicted in Fig. 5. In case of the shorter pulse width of 25τ, the pulse is not long enough for the population to return back down to $n \sim 80$, and the electric field is only strong enough for a time period long enough for the population to reach $n \sim 120$. As the pulse strength diminishes after the peak, the population settles to $n \sim 120$. The fact that by timing the width of pulse we can control the fraction of the population that ends up in either below or above the classical shearless curve is a mere consequence of the drifting of the trajectories in the classical angle coordinate, i.e., the nonzero rotation number. The classical trajectories stay along a line adjacent to the shearless curve as in Fig. 4(d), and the angle coordinate varies with time according to

$$\dot{\theta} = \partial H/\partial J = \frac{1}{2\pi}\partial E/\partial n. \tag{9}$$

Therefore, it vanishes only at the peak in Fig. 3. The direction of drifting is also opposite on the opposite sides of the shearless curve due to the fact that $\partial E/\partial n$ has opposite signs on either side of the peak seen in Fig. 3.

To see this oscillation in time inside the phase space from both classical and quantum-mechanical points of view, we evaluate quantum-mechanical phase-space density in time and plot it against the classical phase-space position of the trajectories at different instances during the driving pulse. We employ the Wigner function to represent the quantum-mechanical phase-space density. Classical action-angle variables correspond to n-angle variables in quantum mechanics since $n = J/2\pi$, and the Wigner function can be defined as (Ref. [14])

$$W(n/2,\theta,t) = \frac{1}{2\pi}\sum_{n'}\psi^*\left(\frac{n+n'}{2},t\right)\psi\left(\frac{n-n'}{2},t\right)e^{-in'\theta}. \tag{10}$$

It has the properties

$$\int_0^{2\pi} W(n/2,\theta,t)d\theta = |\psi(n/2,t)|^2, \tag{11}$$

$$\sum_{n'} W(n/2,\theta,t) = |\psi(\theta,t)|^2, \tag{12}$$

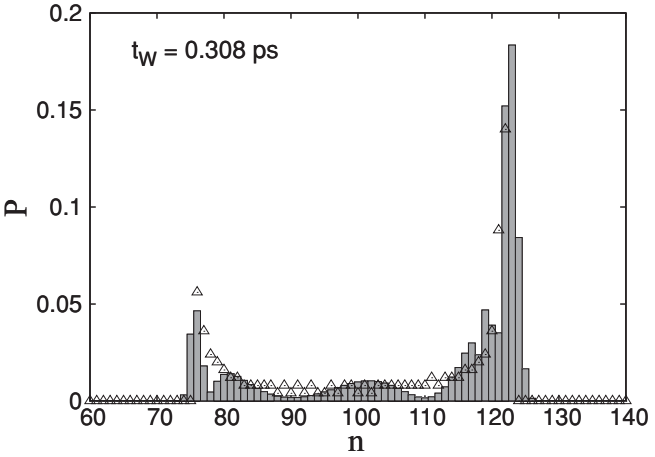

FIG. 8. The final n distributions in Fig. 7 from classical (triangles) and quantum (bars) simulations. Note the excellent agreement between the classical and quantum distributions.

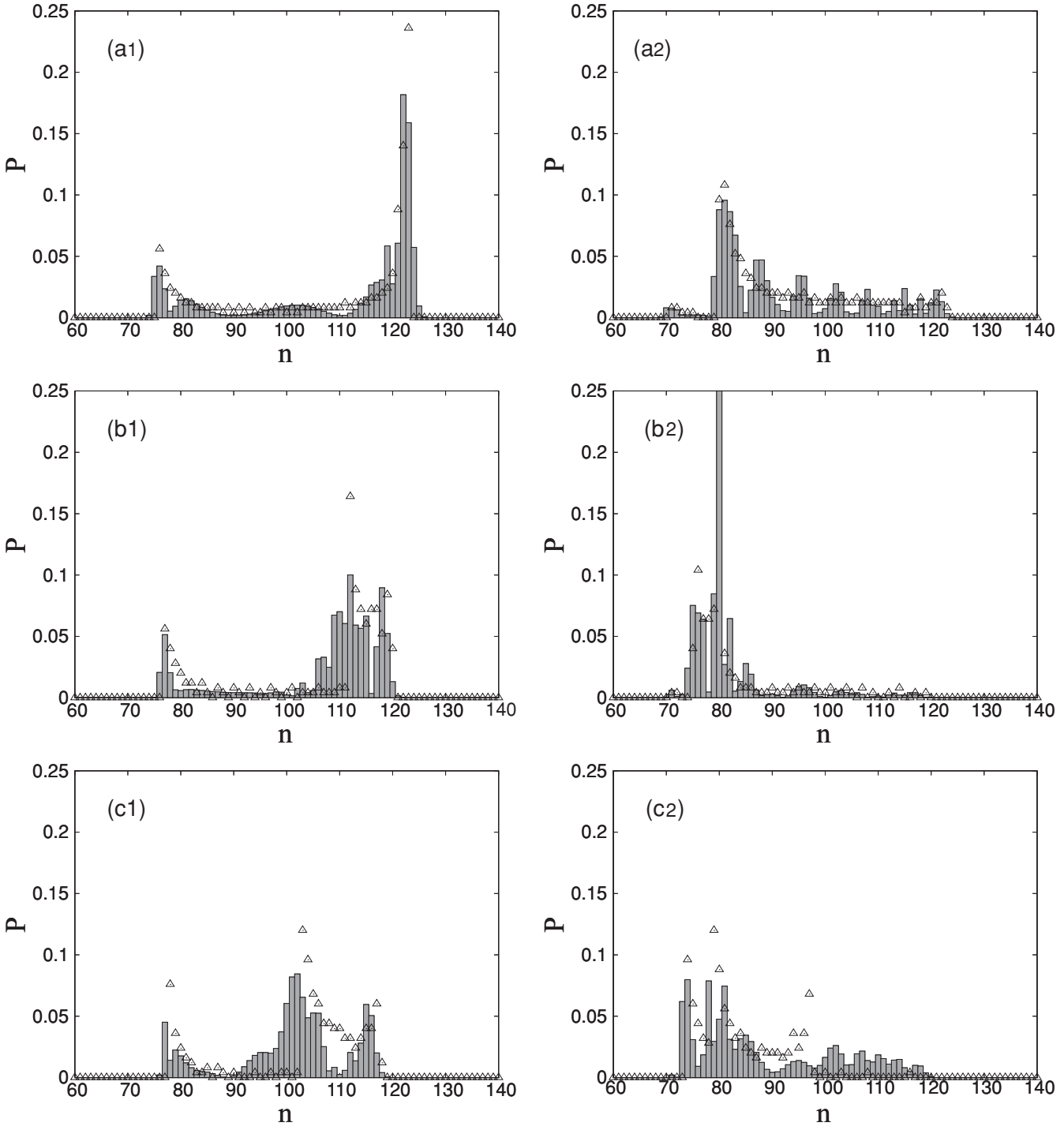

FIG. 9. Final n distributions from classical (triangles) and quantum (bars) simulations for various peak field strengths and pulse widths. The left column has three pulse widths: 25τ (a1), 35τ (b1), and 45τ (c1) all for the peak field strength of 7.0×10^{-5} a.u.. In the left column, the peak field strength is twice as high, 1.4×10^{-4} a.u., and (a2), (b2), and (c2) correspond to the same pulse widths of (a1), (b1), and (c1), respectively. Note that doubling the peak field strength roughly increases the oscillation frequency between $n \sim 80$ and $n \sim 120$ for a given pulse width, and in some cases the quantum simulations display interference patterns which are absent in the classical simulations due to the lack of phase information.

and for an eigenstate $|n_0\rangle$ $W(n,\theta) = \delta_{n,n_0}/2\pi$. It is also periodic as its classical counterpart, $W(n/2,\theta,t) = W(n/2,\theta + 2\pi,t)$.

Figure 7 shows the time evolution of the Wigner distribution overlayed with the classical phase-space positions of the trajectories for the 25τ wide pulse in the lower panel of Fig. 6. As in in Fig. 4, action-angle variables are used to picture the phase space and the point in time during the pulse is displayed in a panel on top of each frame. In the first frame at $t = -0.73$ ps, both quantum-mechanical Wigner function

and the classical phase-space positions lay on top of each other on the $n = 80$ line as the phase space is composed of parallel lines in n since the field has not been turned on yet. As the pulse picks up at $t = -0.27$ ps, the Wigner function has spread out from just a line to a band of n around $n = 80$, and the classical phase-space positions of the trajectories have been distorted from the straight line in the first frame. The peak field strength gets larger as the pulse reaches $t = -0.14$ ps and $t = -0.05$ ps, and the Wigner distribution has spread up in n substantially and reaches $n \sim 100$. Throughout, the classical and quantum distributions show agreement when the shape and maxima of the Wigner function compared with the classical phase-space curve. At $t = 0.09$ ps just after the peak of the pulse, the Wigner function has spread up in n to roughly 120 and its feature corresponding to the classical curve is clearly seen by a π phase shift in the θ coordinate. As the pulse falls, at $t = 0.14$ ps and $t = 0.30$ ps, the tip of the classical curve deforms and extends up in n and the peak of the Wigner function follows it to $n \sim 120$. After the pulse, at $t = 0.56$ ps, both classical and quantum distributions have a wide spread in n, but most of both the Wigner function and the classical trajectories end up along the $n = 120$ line.

The final n distributions in the last frame of Fig. 7 at $t = 1.79$ ps are plotted in Fig. 8 obtained by integrating the phase-space distributions along the θ coordinate. The bars represent the n distribution from the Wigner function and the triangles show the classical distribution. Both peak just above $n = 120$ and spread out in n between roughly the initial state $n = 80$ and $n = 120$, with the classical shearless curve laying right in between the two. It is not a coincidence that both initial and the effective final states are separated from the peak around $n = 100$ in Fig. 3 by exactly 20 states. This is has to do our choice of the driving frequency $\omega_c = 0.0122$ a.u., which was just below the peak in Fig. 3. Recalling the case of the rigid rotor in Fig. 2, multiphoton driving always places the island of stability between the initial and the final states, and as the driving field strength is increased the island gets bigger and finally touches the initial and final states as in Fig. 2(b). This connects the initial state below the island and the final state above it through a separatrix. The only difference in the rigid rotor is that the energy-frequency profile is monotonic and there exists only one island. In the nontwist case, however, there are two islands separated by the shearless curve almost at the driving frequency. As the driving field strength is increased, the islands grow larger and one of them eventually touches the lower initial state below. As in the rigid rotor case, this transports the classical trajectories (or the quantum states) up over the islands, only this time instead of through a heteroclinic separatrix, two separatrices which morph into homoclinic separatrices as the pulse is wept through.

Figure 9 has both the classical and the quantum final n distributions we get when we vary the pulse width and the driving peak field strength independently. As in the previous figure, the bars represent the distribution resulting from our quantum-mechanical simulations, whereas the triangles are from classical calculations. In the first column, the peak field strength is 7.0×10^{-5} a.u. and the pulse widths are 25τ, 35τ, and 45τ at FWHM for (a1), (b1), and (c1), respectively. In the right column, the peak field intensity is twice that in the left column, 1.4×10^{-4} a.u., and the pulse widths are same for each row. Looking at each row independently, doubling the driving field strength while keeping the pulse width fixed roughly doubles the oscillation period of the populations between the initial and the final states. In other words, the speed at which the classical trajectories drift in the θ coordinate in Fig. 7 is higher for higher peak field strength. This results in the faster beating of the classical ensemble as well as the quantum phase-space distribution between above and below the islands as seen in Fig. 5. Going down on a row while keeping the peak field strength fixed in Fig. 9 shows the migration of the final population peak in n as the pulse gets longer. Going from a 25τ wide pulse in (a1) to a 45τ wide pulse in (c1), the population only travels back to $n \sim 100$ from the upper edge at $n \sim 120$. Quantum and classical simulations agree quite well as the triangles closely resemble the distributions expressed by the bar plots, especially for the narrower pulses.

IV. CONCLUSIONS

We have performed classical and quantum-mechanical simulations of population transfer in two physically distinct cases: one in which the frequency of the system monotonically increases with energy and another one where it exhibits an extremum. The first case is referred to as the twist condition and we chose a one-dimensional rigid rotor to demonstrate the classical dynamics that take place in the phase space when we try to transfer population between excited states. The condition where the frequency-energy profile exhibits an extremum is called the nontwist condition and we consider a particle in a one-dimensional potential well with approximately a flat bottom to simulate this condition.

Multiphoton transitions we studied using the one-dimensional rigid rotor, where the frequency of motion changes monotonically with energy, is similar to our previous work involving population transfer in Rydberg atoms driven by microwaves [5], impulsive trains of kicks [7], and diatomic molecules in IR fields [8]. The classical separatrix crossing mechanism we demonstrated in Rydberg atoms is identical to the one we observe in the rigid rotor. At the driving frequency, an island of stability is formed between in the phase space which lays between the initial and the finals states when the phase space is plotted in action-angle variables. As the driving field strength is increased, the island grows larger equally in both up and down directions in action. It eventually touches the initial and the final states connecting them through a separatrix formed by connecting lines in phase space which quantum mechanically would correspond to the initial and final n manifolds.

In the nontwist case, the structure of the classical phase space differs from the one when the frequency changes monotonically with energy, i.e., the rigid rotor. In action-angle variables, we observe two islands of stability separated by a shearless curve, all of which are phase-space structures well studied in nontwist maps [10–12]. Along the shearless curve, the classical frequency is maximum and the trajectories do not drift in the θ coordinate. Further away from the shearless curve, phase-space positions of the trajectories drift faster because the frequency varies more substantially with energy. In other words, the magnitude of dE/dn is larger as one gets further

away from the shearless curve. In case of the rigid rotor, there is no special line at any particular classical action along which dE/dn vanishes.

Driving the nontwist system at a frequency just below the peak of the frequency profile, we are able to transfer an initial microcanonical ensemble of classical trajectories from below the shearless curve to another line above it in phase space, through the line on which the Hamiltonian twist condition is violated. We parallel our classical simulations with one-dimensional quantum calculations and find that classical and quantum mechanics mirror one another in how the dynamical process takes place in phase space. The mechanism at play differs from its counterpart in a system which conforms to the twist condition in that two separatrices form and reconnect as the field strength is increased in the nontwist system. As the field is increased from zero, two homoclinic separatrices form as the islands below and above the shearless curve grow, just like in the rigid rotor. When the field becomes strong enough, these separatrices topologically change and become homoclinic. In the process, the initial ensemble of classical trajectories follow the changing phase-space structure and follow a line that extends from below the lower island to above the upper island. Properly timing the length of the driving pulse, substantial fraction of the population can be made to end up in a final state that is same distance from the initial shearless curve as the initial ensemble of the trajectories.

ACKNOWLEDGMENTS

The authors would like to acknowledge valuable discussions with J. D. Hanson and K. A. Mitchell. This work was supported by the Office of Basic Energy Sciences, US Department of Energy.

[1] C. D. Lin, A. T. Le, Z. Chen, T. Morishita, and R. R. Lucchese, J. Phys. B **43**, 122001 (2010).
[2] J. T. Lin, M. Hayashi, S. H. Lin, and T. F. Jiang, Phys. Rev. A **60**, 3911 (1999).
[3] F. B. Dunning, J. J. Mestayer, C. O. Reinhold, S. Yoshida, and J. Burgdörfer, J. Phys. B **42**, 022001 (2009).
[4] D. J. Maas, D. I. Duncan, R. B. Vrijen, W. J. van der Zande, and L. D. Noordamm, Chem. Phys. Lett. **290**, 75 (1998).
[5] T. Topcu and F. Robicheaux, J. Phys. B **42**, 044014 (2009).
[6] H. Maeda, J. H. Gurian, D. V. L. Norum, and T. F. Gallagher, Phys. Rev. Lett. **96**, 073002 (2006).
[7] T. Topcu and F. Robicheaux, J. Phys. B **43**, 115003 (2010).
[8] T. Topcu and F. Robicheaux, J. Phys. B **43**, 205101 (2010).
[9] V. I. Arnold, *Mathematical Methods of Classical Mechanics* (Springer, New York, 1978).
[10] J. E. Howard and S. M. Hohs, Phys. Rev. A **29**, 418 (1984).
[11] D. del-Castillo-Negrete, J. M. Greene, and P. J. Morrison, Physica D **91**, 1 (1996).
[12] P. J. Morrison, Phys. Plasmas **7**, 2279 (2000).
[13] K. C. Younge, B. Knuffman, S. E. Anderson, and G. Raithel, Phys. Rev. Lett. **104**, 173001 (2010).
[14] Q.-L. Jie, S.-J. Wang, and L.-F. Wei, Phys. Rev. A **57**, 3262 (1998).